

# SCIENTIFIC REPORTS



OPEN

## High-Mobility and High-Optical Quality Atomically Thin WS<sub>2</sub>

Francesco Reale<sup>1</sup>, Pawel Palczynski<sup>1</sup>, Iddo Amit<sup>2</sup>, Gareth F. Jones<sup>2</sup>, Jake D. Mehew<sup>2</sup>, Agnes Bacon<sup>2</sup>, Na Ni<sup>1</sup>, Peter C. Sherrell<sup>1</sup>, Stefano Agnoli<sup>3</sup>, Monica F. Craciun<sup>4</sup>, Saverio Russo<sup>2</sup> & Cecilia Mattevi<sup>1</sup>

Received: 16 June 2017

Accepted: 19 October 2017

Published online: 02 November 2017

The rise of atomically thin materials has the potential to enable a paradigm shift in modern technologies by introducing multi-functional materials in the semiconductor industry. To date the growth of high quality atomically thin semiconductors (e.g. WS<sub>2</sub>) is one of the most pressing challenges to unleash the potential of these materials and the growth of mono- or bi-layers with high crystal quality is yet to see its full realization. Here, we show that the novel use of molecular precursors in the controlled synthesis of mono- and bi-layer WS<sub>2</sub> leads to superior material quality compared to the widely used direct sulfidization of WO<sub>3</sub>-based precursors. Record high room temperature charge carrier mobility up to 52 cm<sup>2</sup>/Vs and ultra-sharp photoluminescence linewidth of just 36 meV over submillimeter areas demonstrate that the quality of this material supersedes also that of naturally occurring materials. By exploiting surface diffusion kinetics of W and S species adsorbed onto a substrate, a deterministic layer thickness control has also been achieved promoting the design of scalable synthesis routes.

Atomically thin layers of metal group VI disulfides and diselenides (MoS<sub>2</sub>, WS<sub>2</sub>, WSe<sub>2</sub>, MoSe<sub>2</sub>) are being extensively investigated as they present unconventional optoelectronic properties compared to commonly used low-dimensional semiconductors<sup>1,2</sup>. In the bulk form they are layered compounds formed of covalently bonded chalcogen and metal atoms forming tri-atomic layers, which are held together by van der Waals forces<sup>3</sup>. An individual tri-atom thick layer presents a direct band gap in the visible-near IR range<sup>4</sup> on the contrary to the bulk, which manifests an indirect electronic band gap. Monolayer sulfides and selenides show strong light absorption from the visible to the near IR range<sup>1,5,6</sup>, valley polarization<sup>7,8</sup>, second-harmonic generation<sup>9</sup>, tightly bound excitons<sup>10</sup> and strong spin-orbit interaction<sup>11,12</sup>. These properties arise from their intrinsic two-dimensional nature inherently free from dangling bonds and their particular d-orbitals configuration<sup>3,13</sup>. Further, given their atomically thin nature they are mechanically flexible and they can sustain tensile strain of 20%<sup>14,15</sup>.

One of the most promising transition metal dichalcogenides (TMDCs) is WS<sub>2</sub> owing to light emission in the monolayer form at ~2 eV and the low level of toxicity of growth processes. Any envisioned application relies on materials with high crystal and optical quality extended over wafer-size areas. Chemical vapour deposition (CVD) is a scalable method for materials synthesis and it is being widely employed for TMDCs<sup>16,17</sup>. The synthesis of tungsten-based materials has revealed to be challenging and generally leading to isolated flakes of lateral size between 5–40 μm<sup>4,18–23</sup>. Monolayer WS<sub>2</sub> films extended over centimeter-sized areas has been demonstrated<sup>24,25</sup>, however with compromised crystal quality as indicated by the low carrier mobilities. The growth is typically performed by co-evaporating sulfur powder and a W-precursor in a horizontal tubular furnace in presence of a carrier gas. Until now, the synthesis of WS<sub>2</sub> has been achieved predominantly using WO<sub>3</sub> and S powders<sup>4,18–23</sup> at temperatures greater than 900 °C. This involves a topotactic-like transformation<sup>26</sup> which normally yields to sparsely distributed WS<sub>2</sub> domains onto an amorphous<sup>4,18,20,22,23</sup> or crystalline substrate<sup>19,21,27</sup>.

Here we demonstrate the synthesis of high quality monolayer WS<sub>2</sub> using carbon-free molecular precursors. The high crystal quality is manifested by the record high charge carrier mobilities of mono- and bi-layer WS<sub>2</sub> and ultra-sharp PL linewidth at room temperature, which are superior to those of naturally occurring materials. The growth is enabled by molecular precursors, which lead to a complete sulfidization of W and formation of WS<sub>2</sub> with lower number of defects compared to the traditionally used direct sulfidization of WO<sub>3</sub>.

<sup>1</sup>Department of Materials, Imperial College, London, SW7 2AZ, UK. <sup>2</sup>Centre for Graphene Science, Department of Physics, University of Exeter, Stocker Road, Exeter, EX4 4QL, UK. <sup>3</sup>Department of Chemical Sciences, University of Padua, Via F. Marzolo 1, 35131, Padua, Italy. <sup>4</sup>Centre for Graphene Science, Department of Engineering, University of Exeter, North Park Road, Exeter, EX4 4QF, UK. Correspondence and requests for materials should be addressed to C.M. (email: [c.mattevi@imperial.ac.uk](mailto:c.mattevi@imperial.ac.uk))

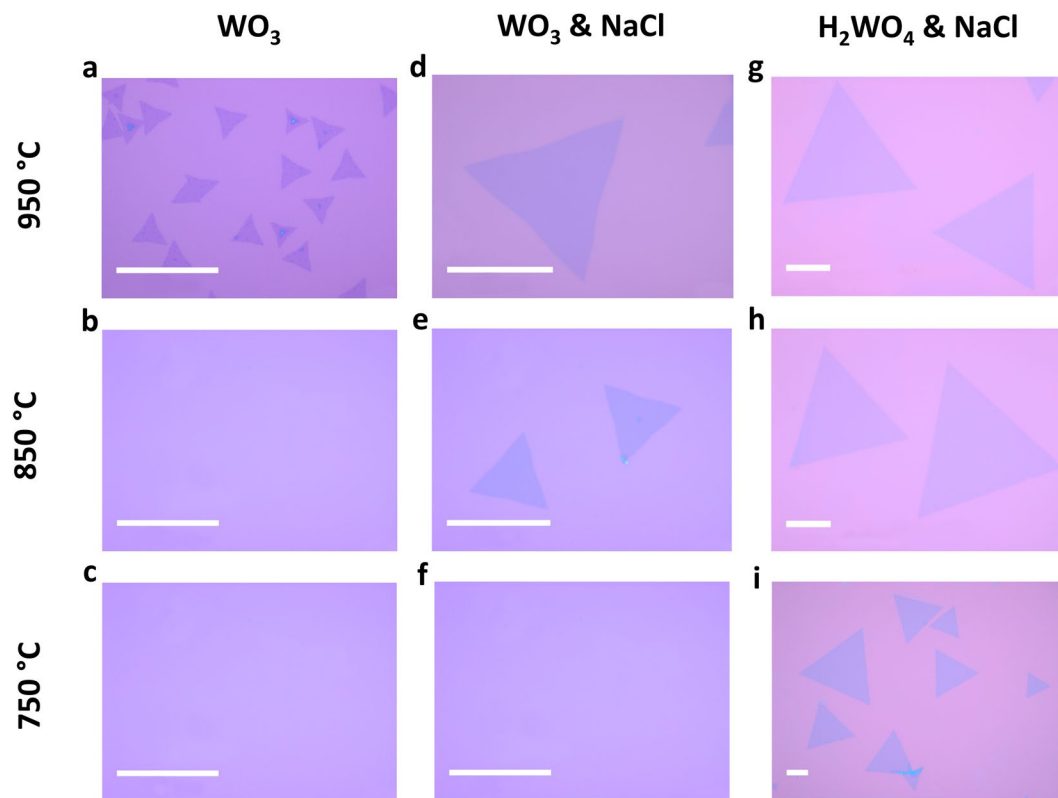


**Figure 1.** Optical micrographs of WS<sub>2</sub> triangles grown on SiO<sub>2</sub>/Si substrates at different temperatures and using different precursors: (a) WO<sub>3</sub> at 950 °C; (b) WO<sub>3</sub> at 850 °C; (c) WO<sub>3</sub> at 750 °C; (d) WO<sub>3</sub> + NaCl at 950 °C; (e) WO<sub>3</sub> + NaCl at 850 °C; (f) WO<sub>3</sub> + NaCl at 750 °C; (g) H<sub>2</sub>WO<sub>4</sub> + NaCl at 950 °C; (h) H<sub>2</sub>WO<sub>4</sub> + NaCl at 850 °C; (i) H<sub>2</sub>WO<sub>4</sub> + NaCl at 750 °C. Scale bar is 50 μm.

## Results and Discussion

The synthesis of WS<sub>2</sub> was performed starting from commercial powders of either H<sub>2</sub>WO<sub>4</sub> (hydrated tungsten oxide) or WO<sub>3</sub>, sulfur and where indicated, we have introduced NaCl. W and S precursors were placed in two separate crucibles well-spaced in a quartz tubular furnace (Supporting Information, Figure S1a) and heated up independently using different controllers as reported in Figure S1b. The heating profile of S powders has been optimized to ensure maximum supply when the W-precursors start evaporating. WS<sub>2</sub> was grown on Si/SiO<sub>2</sub> (285 nm) substrates loaded in the downstream zone of the tubular furnace. Altering the chemistry of decomposition of tungsten oxide species, we could achieve synthesis of monolayer WS<sub>2</sub> over larger area coverage, at low temperatures and with low amount of defects.

Optical micrographs of WS<sub>2</sub> monolayers (Fig. 1) grown using different tungsten oxide precursors systems at different temperatures (950 °C, 850 °C and 750 °C) show distinctively increasing lateral size of the triangles and increasingly facilitated synthesis at low temperatures from WO<sub>3</sub> to WO<sub>3</sub>-NaCl and H<sub>2</sub>WO<sub>4</sub>-NaCl. The possibility to grow WS<sub>2</sub> from WO<sub>3</sub> at temperatures not lower than 950 °C is notoriously attributed to the high sublimation temperature of the oxide<sup>17,28–30</sup>. In specific, the size of the WS<sub>2</sub> triangles increases from ~10 μm, to 60 μm, upto 200 μm with areas of continuous polycrystalline monolayered coverage of ~0.8 mm (Figure S2). Further, the WS<sub>2</sub> synthesis at temperatures as low as 750 °C was enabled only by the precursors system of H<sub>2</sub>WO<sub>4</sub>-NaCl with remarkable triangular size of ~100 μm. In addition, increasing the growth pressure (from ~1 mbar to 13 mbar) at 950 °C, bilayered WS<sub>2</sub> flakes are preferentially formed (Figure S3) using the H<sub>2</sub>WO<sub>4</sub>-NaCl system.

It is worth noting that larger WS<sub>2</sub> domains obtained at 950 °C, as compared to 850 and 750 °C, can be explained in the light of the Robinson & Robin model<sup>31</sup>. At high temperature the diffusivity of the adsorbed precursors on the SiO<sub>2</sub> surface is favourable leading to the expansion of the existing domains. At the same time, desorption of absorbed species is higher than at lower temperatures, limiting the achievement of a supersaturation concentration and thus reducing the nucleation density.

From structural investigation of the reaction products in the different precursors systems, we could elucidate the role played by the water intercalated in the H<sub>2</sub>WO<sub>4</sub> and how this can enable the favorable synthesis at low temperature and with low density of defects as compared to the WO<sub>3</sub>-based precursors. From X-ray diffraction (XRD) characterization (Supporting Information) it was possible to observe that the main products of the reactions between NaCl and either H<sub>2</sub>WO<sub>4</sub> or WO<sub>3</sub> are similar: Na<sub>x</sub>W<sub>y</sub>O<sub>z</sub> and tungsten oxychlorides (WClO<sub>4</sub> and WO<sub>2</sub>Cl<sub>2</sub>). However the reactions occur at significantly lower temperatures for H<sub>2</sub>WO<sub>4</sub> compared to WO<sub>3</sub>. While Na<sub>x</sub>W<sub>y</sub>O<sub>z</sub> species possesses a high evaporation temperature, as they are found in the crucible (Figure S5) at the end of the synthesis of WS<sub>2</sub>, the tungsten oxychlorides are volatile (Figures S4, S5) and they can possibly play a key role in promoting the synthesis of WS<sub>2</sub>. Indeed the system H<sub>2</sub>WO<sub>4</sub>-NaCl is likely to enable the formation of

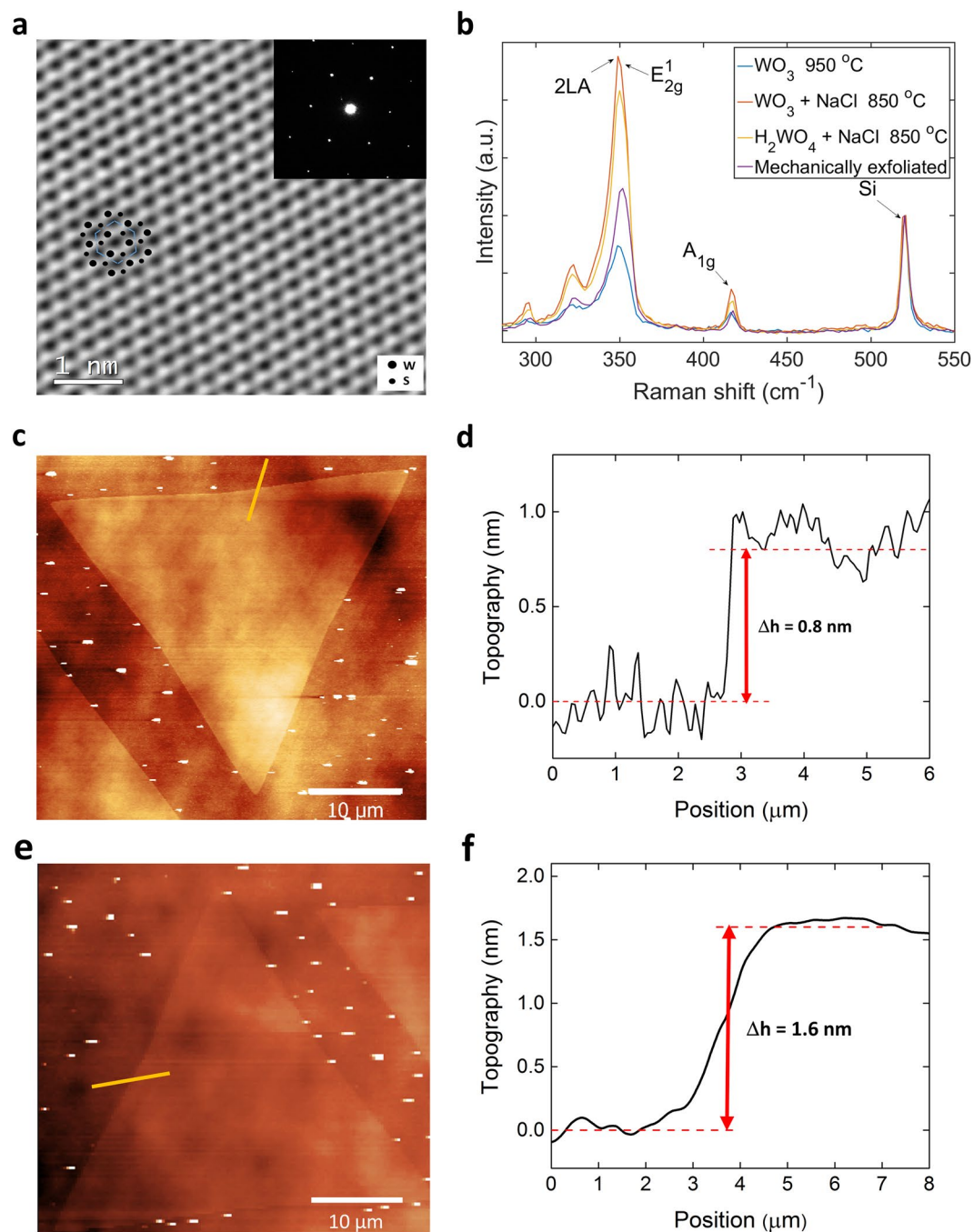


**Figure 2.** Structural and physical characterization of WS<sub>2</sub> triangles: (a) Phase image of the reconstructed exit-plane wave function from a focal-series of HRTEM images of the WS<sub>2</sub> lattice grown using H<sub>2</sub>WO<sub>4</sub> + NaCl. The inset reports a selected diffraction area which shows an hexagonal pattern; (b) Raman spectra showing the characteristics active modes of WS<sub>2</sub> grown under different conditions and compared with mechanically exfoliated flakes; (c) AFM image and (d) corresponding thickness profile of monolayer WS<sub>2</sub>; (e) AFM image and (f) corresponding thickness profile of bilayer WS<sub>2</sub>.

tungsten-oxyhalide species (i.e., WO<sub>2</sub>Cl<sub>2</sub>, WOCl<sub>4</sub>) at lower temperatures than WO<sub>3</sub>-NaCl, as NaCl dissociation is promoted by the H<sub>2</sub>O molecules gradually released by H<sub>2</sub>WO<sub>4</sub> upon heating. On the bases of previous studies on the synthesis of WS<sub>2</sub> bulk crystals, the formation of tungsten oxychlorides (WO<sub>2</sub>Cl<sub>2</sub> and WOCl<sub>4</sub>) is indeed likely to occur with higher chances with respect to the formation of metal halides (e.g. WCl<sub>6</sub>)<sup>32,33</sup>. Tungsten oxychlorides (WO<sub>2</sub>Cl<sub>2</sub> and WOCl<sub>4</sub>) can be volatile from 200 °C<sup>34</sup> and they can be sulfidized in vapour phase forming a few-atom clusters of W-S which can deposit onto the target substrate as adatom species<sup>35</sup> where they can form WS<sub>2</sub> via a diffusion-desorption mediated mechanism of nucleation and growth. WOCl<sub>4</sub> has been previously used<sup>36</sup> as precursor for the synthesis of WS<sub>2</sub> bulk films. Despite its strong tungsten-oxygen double bonds, WOCl<sub>4</sub> proved to be an effective precursor with a clean decomposition pathway without formation of tungsten

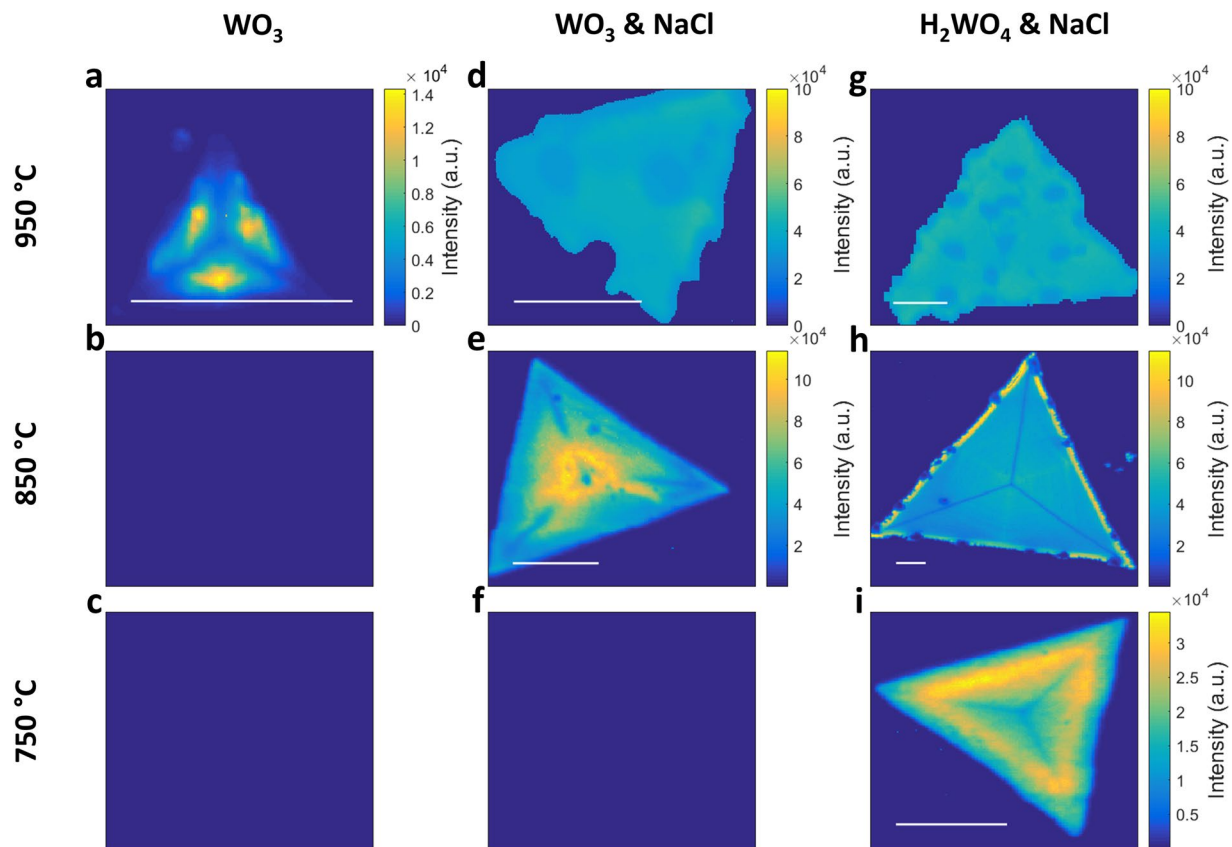


**Figure 3.** Spatial maps of PL intensity of  $\text{WS}_2$  grown in the conditions exemplified in Fig. 1. The scale bar length is  $10\ \mu\text{m}$ .

oxysulfides. We have verified that using this precursor is indeed possible to obtain  $\text{WS}_2$  at temperatures as low as  $550\ \text{°C}$  (Figure S6a). The key role played by the oxyhalide species becomes apparent if we try to grow  $\text{WS}_2$  by using  $\text{H}_2\text{WO}_4$  as single precursor. As this decomposes to form  $\text{WO}_3$ , only small  $\text{WS}_2$  domains are observed with PL characteristics similar to the  $\text{WO}_3$  precursor-led growth (Figure S6b).

High-resolution transmission electron microscopy (HRTEM) imaging confirms the high crystalline nature of the material (Fig. 2a). The measured lattice constant is  $\sim 0.3\ \text{nm}$  consistent with that of  $2\text{H-WS}_2$  ( $a = 0.318\ \text{nm}$ ). The Raman spectra of  $\text{WS}_2$  obtained using the different precursors systems are shown in Fig. 2b. All of the spectra exhibit two characteristic peaks located at  $\sim(351 \pm 0.53)\ \text{cm}^{-1}$  and  $\sim(417.6 \pm 1)\ \text{cm}^{-1}$ , which can be attributed to  $2\text{LA-E}^1_{2g}$  and  $\text{A}^1_{1g}$  Raman modes of pristine  $\text{WS}_2$  monolayer<sup>37,38</sup>. Interestingly, the distribution of the peak positions is increasingly narrower from  $\text{WO}_3$  precursor,  $\text{WO}_3 + \text{NaCl}$  and to  $\text{H}_2\text{WO}_4 + \text{NaCl}$  (Figures S8, S10). The Raman peaks intensities are uniform across the entire triangle area (Figures S7, S9) and the frequency difference ( $\Delta\nu$ ) between  $2\text{LA}(M)$  and  $\text{A}^1_{1g}$  modes is  $\sim(66.5 \pm 0.53)\ \text{cm}^{-1}$  (Figure S11), as expected for monolayer  $\text{WS}_2$ <sup>37</sup>. The AFM thickness profile analysis of  $\text{WS}_2$  triangles confirms the monolayer (Fig. 2c,d) and bilayer (Fig. 2e,f) nature of the flakes, showing an edge step height of  $\sim 0.8\ \text{nm}$  (Fig. 2d) and  $\sim 1.6\ \text{nm}$  (Fig. 2f), respectively<sup>39,40</sup>.

A comparison of representative photoluminescence (PL) intensity maps of  $\text{WS}_2$  monolayers grown under the three precursors systems at different temperatures is reported in Fig. 3. The PL peak intensity appears consistently higher for the NaCl-based precursors system as compared to  $\text{WO}_3$ . The intensity variation pattern across an individual flake is not yet fully understood<sup>41</sup>, and it is likely to be due to different defect concentrations in the form of sulfur vacancies. The FWHM of the PL peaks significantly decreases from  $\sim 75\ \text{meV}$ , to  $\sim 50\ \text{meV}$ , to  $\sim 36\ \text{meV}$  for the three precursors systems,  $\text{WO}_3$ ,  $\text{WO}_3 + \text{NaCl}$ , and  $\text{H}_2\text{WO}_4 + \text{NaCl}$  respectively, with a distribution significantly narrower and more uniform across the same flake and different flakes (SI). It is worth noting that  $36\ \text{meV}$  of FWHM is narrower than mechanically exfoliated material (Fig. 4a) which is  $\sim 59\ \text{meV}$ . This suggests that  $\text{WS}_2$  grown by using  $\text{H}_2\text{WO}_4 + \text{NaCl}$  possesses less structural defects compared to the other precursors systems, and specifically in the form of sulfur vacancies. Indeed, it has been reported that S vacancies increase the electron density, thus the trions population and the strength of the PL emission at lower energies than the optical band gap with a consequent increase of the FWHM<sup>4,42</sup>. The PL peak position progressively blueshifts from  $1.94\ \text{eV}$ , to  $1.96\ \text{eV}$ , to  $1.98\ \text{eV}$ , reaffirming a decreased amount of S vacancies and the formation of a progressively more pristine material.

A molecular conversion based-growth mechanism, where tungsten oxyhalide molecules are sulfidized in vapour phase, versus a topotactic-like conversion of  $\text{WO}_3$  in  $\text{WS}_2$  can explain the different defects contents in  $\text{WS}_2$ . The greater efficiency of  $\text{H}_2\text{WO}_4$  in inducing a complete sulfidization of the precursors compared with the  $\text{WO}_3 + \text{NaCl}$  system has been also confirmed by chemical analysis (X-ray photoelectron spectroscopy). Analysing

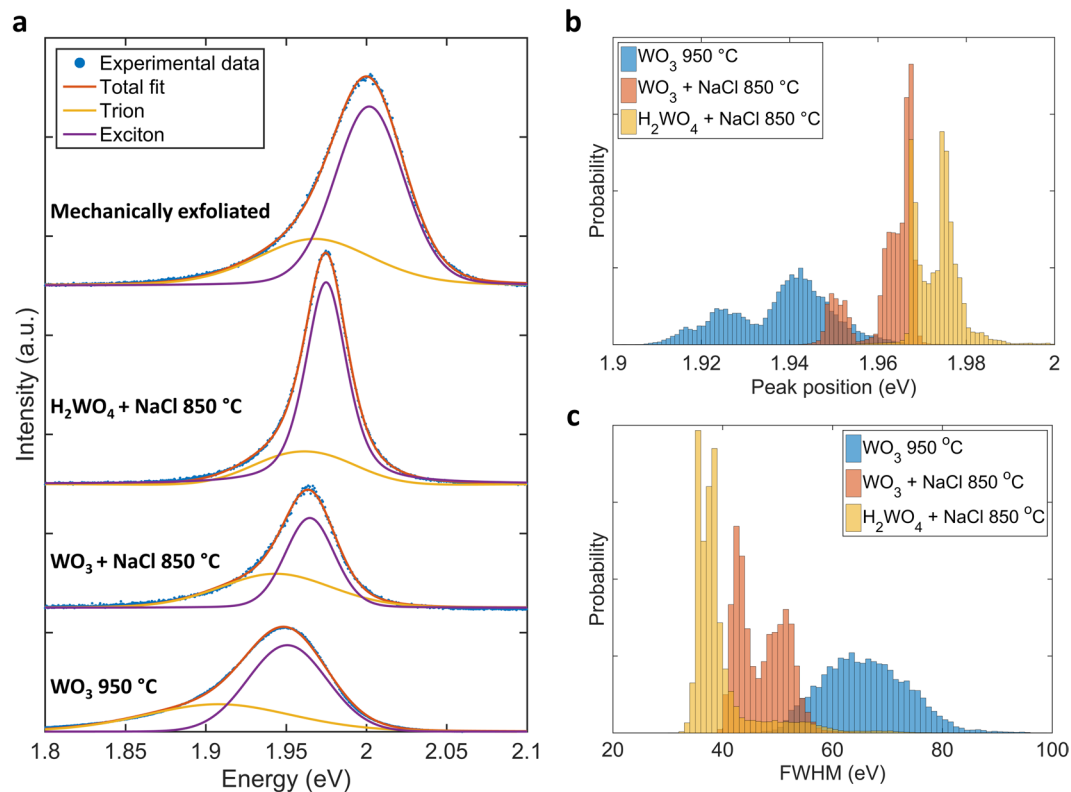


**Figure 4.** PL spectra characteristics of  $\text{WS}_2$  grown using:  $\text{WO}_3$  at  $950^\circ\text{C}$ ,  $\text{WO}_3 + \text{NaCl}$  at  $850^\circ\text{C}$ ,  $\text{H}_2\text{WO}_4 + \text{NaCl}$  at  $850^\circ\text{C}$ : (a) individual spectra (dotted line) and deconvolution in exciton and trion components; (b) distribution of PL peak position and (c) distribution of PL FWHM for several  $\text{WS}_2$  monolayers grown using the three different precursors systems.

$\text{WS}_2$  grown using  $\text{H}_2\text{WO}_4 + \text{NaCl}$ , the  $\text{W } 4f_{5/2}$  and  $\text{W } 4f_{7/2}$  core levels (Fig. 5a) present peak position characteristic of  $\text{W}^{4+}$  in  $\text{WS}_2$ <sup>43,44</sup> (32.7 and 34.8 eV respectively) and the narrowest achievable FWHM (1 eV) (Fig. 5a), using the  $\text{Mg K}\alpha$  as X-ray source. This indicates chemical purity and expected stoichiometric ratio of W and S. This has been also confirmed by calculating the concentration of S and W from the integrated intensity of the W 4f and S 2p core levels. The S  $2p_{1/2}$  and  $2p_{3/2}$  core levels, also appear at the expected position for  $\text{WS}_2$  (162.3 eV and 163.4 eV respectively, Figure 5b)<sup>44</sup> and with a very narrow FWHM (1 eV) (Fig. 5c). A very small amount of  $\text{W}^{6+}$  ( $\text{W } 4f_{5/2}$  and  $\text{W } 4f_{7/2}$  core levels centred at 35.9 eV and 38.1 eV respectively in Fig. 5a) attributable to  $\text{WO}_3$ , which partially overlaps with the W 5p core level (38.5 eV), can be observed which however disappears after transferring the flakes on a new  $\text{SiO}_2/\text{Si}$  substrate (Fig. 5c) and thus suggesting that it is related to residual precursors on the substrate considering the XPS spot size is  $\sim 1$  mm. It is worth noting that after transfer the FWHM of the W 4f core levels remains unchanged suggesting that the transfer process preserves the crystallinity of the flakes and no additional defects are introduced.

Similarly, chemical purity and expected stoichiometric ratio of 2:1 for S:W have been observed for  $\text{WS}_2$  grown from  $\text{WO}_3 + \text{NaCl}$  (Fig. 5a). Nevertheless, a larger  $\text{W}^{6+}$  contribution, attributable to  $\text{WO}_3$  ( $\text{W } 4f_{5/2}$  and  $\text{W } 4f_{7/2}$  centred at 35.9 eV and 38.1 eV respectively in Fig. 5a) has been detected in this case suggesting that a conspicuous amount of precursors does not get sulfurized and it is just deposited onto the  $\text{SiO}_2$  wafer. Upon transfer on a new  $\text{SiO}_2/\text{Si}$  substrate, this component entirely disappears (Fig. 5c), thus indicating also in this case that  $\text{WO}_3$  is mainly distributed on the substrate. The FWHM of the  $\text{W}^{4+}$  4f core levels is  $\sim 1.2$  eV in this case, suggesting higher concentration of defects compared to  $\text{H}_2\text{WO}_4 + \text{NaCl}$ -led growth (Fig. 5a). The transferred  $\text{WS}_2$  present a FWHM even larger  $\sim 1.3$  eV, suggesting the introduction of atomic defects as a consequence of the mechanical stress underwent by the flakes with preexisting defects (Fig. 5c). To conclude, XPS study confirms the effectiveness of  $\text{H}_2\text{WO}_4$  as precursor versus  $\text{WO}_3$ .

The progressive reduction of structural defects from  $\text{WO}_3$  to  $\text{H}_2\text{WO}_4$  has been proven by electrical characterization. The electrical properties of the  $\text{WS}_2$  flakes were characterised through their performance in bottom-gated field effect transistors (FET) (Fig. 6a,b). The FET transfer curve (Fig. 6c) displays an accumulation-type *n*-channel transistor, where the current flowing through the channel increases with increased gate bias, after the threshold voltage.

The field-effect mobility was calculated in the linear region of the transport graph (marked with red-dashed line in Fig. 6c), using  $\mu_n = C_{\text{ox}}^{-1}(d\sigma/dV_{\text{gs}})$ . Overall, monolayer  $\text{WS}_2$  grown using  $\text{H}_2\text{WO}_4 + \text{NaCl}$  shows electron mobilities systematically higher compared with the  $\text{WO}_3 + \text{NaCl}$  system (Fig. 6c,e,f) corroborating the fact that higher crystal quality is expected by using  $\text{H}_2\text{WO}_4$  as precursor. Further, monolayer  $\text{WS}_2$  presents electron mobility of  $\sim (28 \pm 1.4) \text{ cm}^2/\text{Vs}$  (Fig. 6c,f) which is the highest mobility reported so far for CVD grown  $\text{WS}_2$  deposited

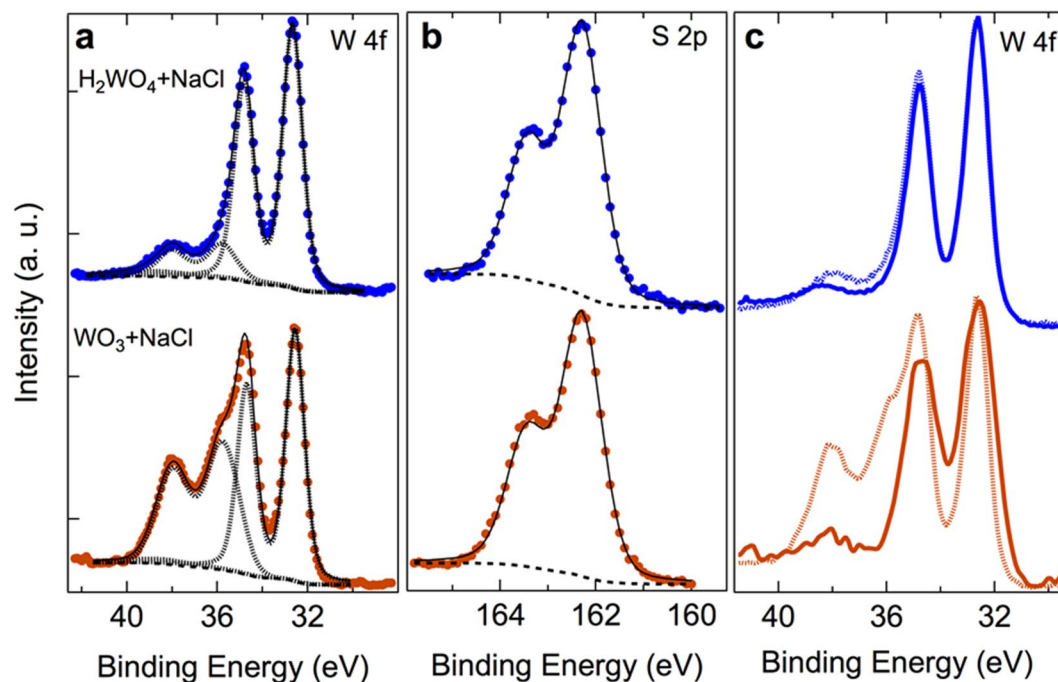


**Figure 5.** XPS spectra of the W 4f and S 2p core level peak regions. (a) Comparison of W  $4f_{5/2}$ , W  $4f_{7/2}$  and W 5p core levels of WS<sub>2</sub> grown using H<sub>2</sub>WO<sub>4</sub> + NaCl at 950 °C (blue spectrum) with WS<sub>2</sub> grown using WO<sub>3</sub> + NaCl at 950 °C (red spectrum). The deconvolution of W  $4f_{5/2}$ , W  $4f_{7/2}$  and W 5p core levels and overall fit of the spectrum are reported as black dashed and a continuous line respectively. (b) The S 2p<sub>1/2</sub> and 2p<sub>3/2</sub> core levels for each of the two growth conditions are reported in the central panel. (c) W  $4f_{5/2}$ , W  $4f_{7/2}$  and W 5p core levels before (dashed line) and after transfer (continuous line) onto a new SiO<sub>2</sub>/Si substrate are compared showing the complete disappearance of the residual WO<sub>3</sub> components. The spectra were fit by Doniach-Sunjic function after subtracting a Shirley background (black dashed line).

onto SiO<sub>2</sub> (Fig. 7a)<sup>19,21,23–25,30,45–49</sup> and comparable to mechanically exfoliated WS<sub>2</sub><sup>37,50–52</sup>. The highest mobilities using either H<sub>2</sub>WO<sub>4</sub> + NaCl or WO<sub>3</sub> + NaCl are displayed at 950 °C (Fig. 6f) suggesting that the growth temperature does also play a role in improving the crystal quality of the material. While the role played by the different precursors systems in determining the crystallinity of the synthesis product becomes more prominent at low growth temperatures. Monolayer WS<sub>2</sub> grown using H<sub>2</sub>WO<sub>4</sub> + NaCl exhibits electron mobilities of  $\sim(10 \pm 1)$  cm<sup>2</sup>/Vs at temperatures between 750 °C and 900 °C. While the electron mobilities of monolayer WS<sub>2</sub> grown using WO<sub>3</sub> + NaCl at 850 °C (Fig. 6f) present lower values of  $\sim(0.4 \pm 0.1)$  cm<sup>2</sup>/Vs. Bilayer WS<sub>2</sub> shows electron mobility systematically higher than monolayer and also systematically higher than mechanically exfoliated bilayered flakes<sup>52,53</sup> (Fig. 7b). The electron mobility of  $\sim(52 \pm 4)$  cm<sup>2</sup>/Vs (Figs 7b, 8a,b,c) represents a record mobility as compared to CVD grown or mechanically exfoliated bilayer WS<sub>2</sub> onto SiO<sub>2</sub> reported so far<sup>52–54</sup>. The fact that the highest mobility for bilayer WS<sub>2</sub> has been obtained using WO<sub>3</sub> + NaCl with no use of H<sub>2</sub>WO<sub>4</sub> suggests that the bilayer system is less affected by the precursors choice, and a bilayered material presents in general crystal quality superior to monolayers.

## Conclusions

In conclusion, we have developed a synthesis strategy which enables high crystal quality WS<sub>2</sub> as reflected in the high optical quality and in the carrier mobility that overcome naturally occurring materials. The molecular precursors approach leads to effective sulfidization of W, revealing to be highly advantageous with respect to the traditional oxide-based conversion synthesis of WS<sub>2</sub>. These results can be translated and applied to the synthesis of different TMDCs, and pave the way towards industrially scalable synthesis of monolayer WS<sub>2</sub> over large areas.

## Methods

**CVD Synthesis of WS<sub>2</sub>.** Commercial WO<sub>3</sub> (0.3 g, 99.9%, Sigma Aldrich), H<sub>2</sub>WO<sub>4</sub> (0.3 g, 99.9%, Sigma Aldrich) and NaCl (0.3 g,  $\geq 99.5\%$ , Sigma Aldrich) powders were loaded in an alumina boat placed in the center of a 2 inch-diameter horizontal quartz tube CVD furnace. While an alumina boat containing sulfur powders (0.6 g,  $\geq 99.5\%$ , Sigma Aldrich) was loaded in the upstream zone of the tube, whose temperature was independently controlled by a different heater. The growth substrates were Si wafers (500 microns) with on top 285 nm of SiO<sub>2</sub> thermally deposited. The substrates were sequentially cleaned for 15 min in acetone, isopropanol and deionized water in a sonicator, followed by dipping in H<sub>2</sub>SO<sub>4</sub>/H<sub>2</sub>O<sub>2</sub> (3:1) for two hours and rising in deionized water. They were then blow dried with nitrogen gas, cleaned with O<sub>2</sub> plasma for 5 min and loaded into the downstream zone of the furnace. The CVD growths were then performed at low pressure ( $\sim 10^{-1}$  mbar) and under flow of high

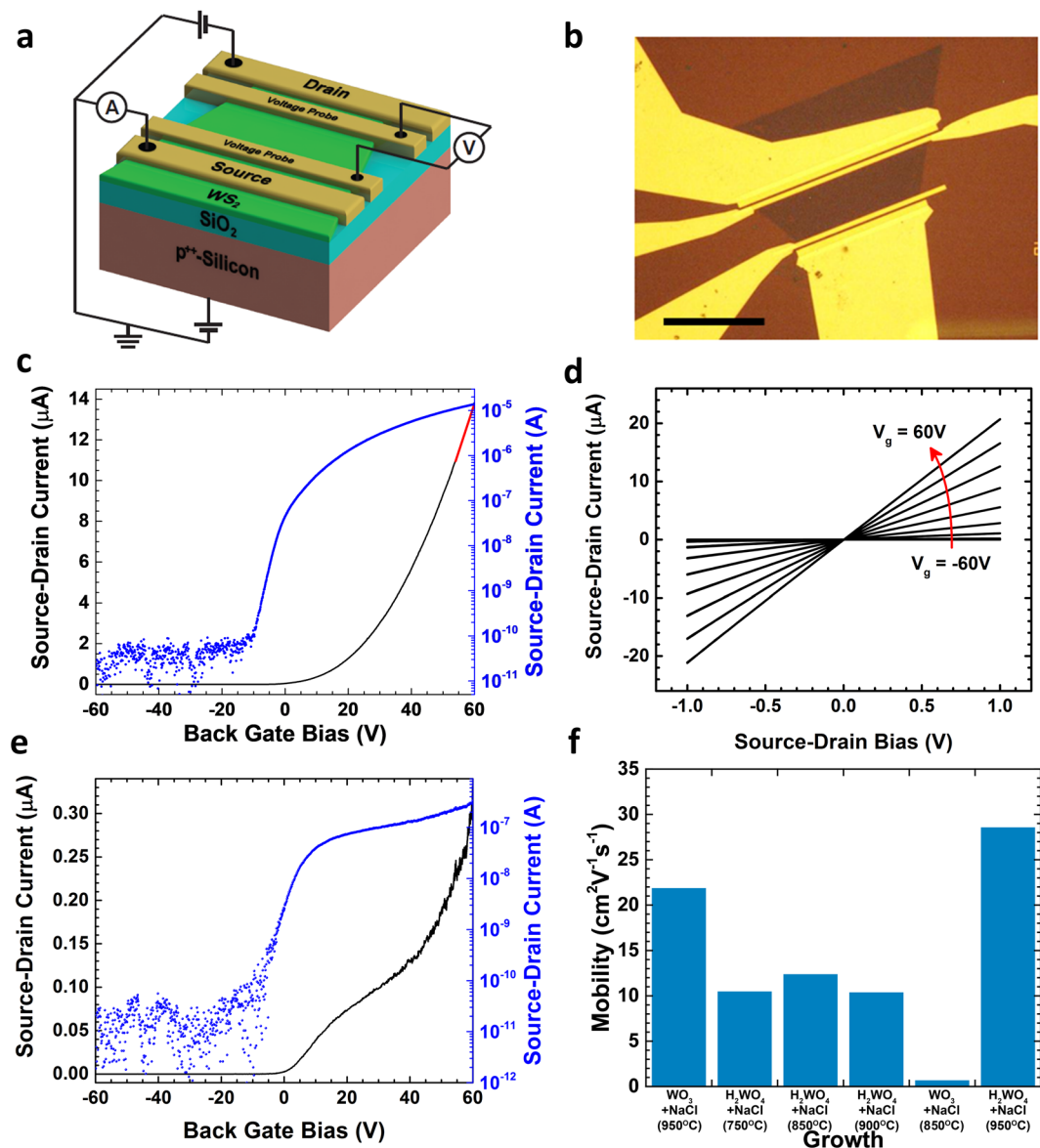


**Figure 6.** Electrical characteristics of monolayer WS<sub>2</sub>: (a) Schematic of the bottom-gated field effect transistors; (b) optical micrograph of the device (scale bar is 20 μm); (c) FET transfer curve for the monolayer WS<sub>2</sub> grown using H<sub>2</sub>WO<sub>4</sub> + NaCl at 950 °C showing the highest mobility of 28 cm<sup>2</sup>/Vs (linear region of the transport graph marked with a red-dashed line); (d) Response curves at different gate biases for a WS<sub>2</sub> triangle grown using H<sub>2</sub>WO<sub>4</sub> + NaCl; (e) FET transfer curve for the monolayer WS<sub>2</sub> grown using WO<sub>3</sub> + NaCl at 850 °C; (f) electron mobilities of monolayers WS<sub>2</sub> grown using different conditions.

purity Ar gas (flow rate of 100 sccm). The furnace was heated to 750–950 °C with a ramp rate of 25 °C min<sup>-1</sup>, kept at the growth temperatures for 15 min and then naturally cooled down to room temperature. The sulfur powder was independently heated to 125 °C with a ramp of 5 °C min<sup>-1</sup>, kept at this temperature for 15 min and naturally cooled down.

**Sample Transfer.** The transfer procedure was performed by depositing a PMMA film 350 nm thick onto the target sample, which was subsequently immersed in a KOH solution (0.1 M) until detachment of the PMMA from the SiO<sub>2</sub>/Si substrate. The PMMA/WS<sub>2</sub> films was then scooped out with a new Si/SiO<sub>2</sub> substrate, repeatedly washed in deionized water and then immersed in an acetone bath at 45 °C for 20 min to dissolve the PMMA film.

**TEM Characterization.** TEM analysis of the WS<sub>2</sub> flakes was carried out on a FEI Titan 80–300 S/TEM operated at 80 kV, equipped with a monochromator and a Cs aberration image corrector. Focal series micrographs of the representative flake were acquired at different objective lens focus values (using a spherical aberration coefficient Cs ~ -4 μm) and exit-wave reconstruction was performed using TrueImage software (FEI).

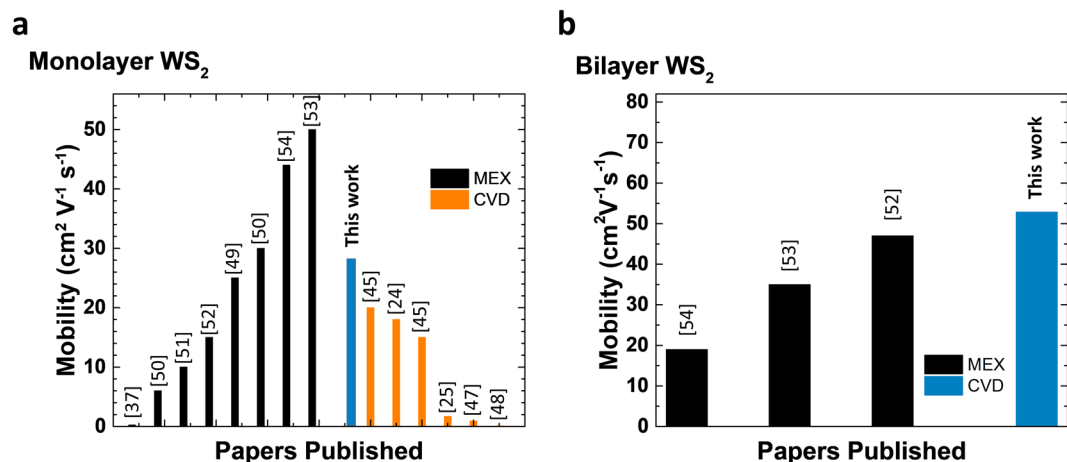


**Figure 7.** Comparison of our results with the literature of CVD grown material and mechanically exfoliated WS<sub>2</sub> (MEX): electron mobility for (a) monolayer WS<sub>2</sub> and (b) bilayer WS<sub>2</sub>. The histograms show our record values for both monolayer and bilayer amongst the best values reported for CVD grown WS<sub>2</sub>.

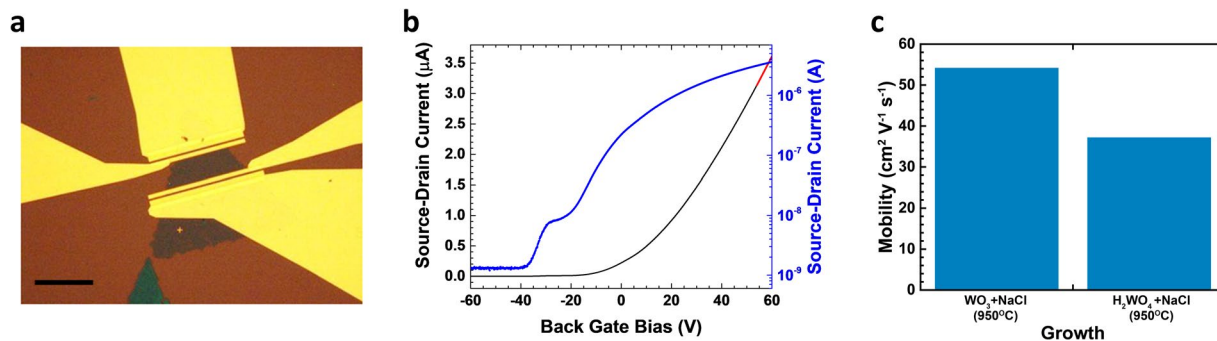


**Figure 8.** Electrical characteristics of bilayer WS<sub>2</sub>: (a) Optical micrograph of the device (scale bar is 30 μm); (b) FET transfer curve for the bilayer WS<sub>2</sub> grown using WO<sub>3</sub> + NaCl at 950 °C showing the highest mobility of 52 cm<sup>2</sup>/Vs (linear region of the transport graph marked with a red-dashed line); (c) electron mobility of bilayer WS<sub>2</sub> grown by using different precursors systems.

**Physical Characterization.** Raman and photoluminescence spectra were collected using a Renishaw inVia spectrometer equipped with a 532 nm laser excitation. All the spatial maps were collected under a 100x objective using grating of 1800 line/mm, which provide a resolution of ~1.5 cm<sup>-1</sup>.

**X-ray Photoelectron Spectroscopy.** X-Ray photoemission spectra were acquired in a custom made ultra-high vacuum system (pressure < 10<sup>-9</sup> mbar) equipped with a VG Escalab Mk-II electron analyzer and a twin anode (Al/Mg) non-monochromatized x-ray source (Omicron DAR 400). All measurements were taken in quasi-normal emission (5° off) at room temperature using a pass-energy of 20 eV, an energy step of 0.1 eV and the Mg K<sub>α</sub> emission line as exciting radiation.

**Device Fabrication.** For the field-effect mobility measurements, single and bilayer WS<sub>2</sub> field-effect transistors (FET) were fabricated after transfer to a new Si/SiO<sub>2</sub> substrate where the Si is highly *p*-doped and acts as a global gate electrode, and a 285 nm thick thermally grown SiO<sub>2</sub> serves as the gate dielectric. The FETs were fabricated on dried Si/SiO<sub>2</sub>/WS<sub>2</sub> samples. Besides the current bearing contacts, termed here “Source” and “Drain”, two additional voltage probes were added to each FETs to allow for an accurate determination of the channel’s conductance by eliminating the contribution of the contacts. Both the current bearing leads and the voltage probes were patterned simultaneously using a standard electron beam lithography process. The source, drain and voltage probes consisted of 50 nm Au, while the electronics leads consisted of 5 nm Ti and 50 nm Au. A two-steps annealing process followed the fabrication. The samples were first annealed for 2 hours at 200 °C under H<sub>2</sub>/Ar (10/90) flow in atmospheric pressure, to etch residues of PMMA that was used as an electron resist for the lithography step. Then, the samples were put under a high vacuum (~10<sup>-6</sup> mbar) and baked at 115 °C for 60 hours, to promote desorption of water molecules from the channel surface.

**Electrical Measurements.** The FETs were measured inside the vacuum chamber at a constant pressure of  $\sim 10^{-6}$  mbar, without exposure to ambient conditions after the second annealing step. The drain electrode was biased with a low noise source-meter and the source electrode was grounded throughout the experiment. An additional source-meter was used to bias the global gate electrode, with respect to the source. The transistor current,  $I_{ds}$ , was measured using an ammeter and the potential difference across the voltage probes,  $V_{A-B}$ , was measured with a voltmeter. The channel conductivity,  $\sigma$ , is then readily obtained using  $\sigma = (L I_{ds}) / (W V_{A-B})$ , where  $W$  and  $L$  are the channel's width and length, respectively. The measurement set-up is shown schematically (not to scale) in Fig. 6a. The oxide capacitance was estimated to be  $115 \mu\text{Fm}^{-2}$  from  $C_{ox} = \epsilon_0 \epsilon_r / d_{ox}$ , where  $d_{ox}$  is the oxide thickness and  $\epsilon_0$  and  $\epsilon_r$  are the vacuum permittivity and  $\text{SiO}_2$  relative permittivity, respectively.

**Data availability statement.** All relevant data generated or analysed during this study are included in this article and its Supplementary Information file.

## References

- Mak, K. F., Lee, C., Hone, J., Shan, J. & Heinz, T. F. Atomically thin  $\text{MoS}_2$ : a new direct-gap semiconductor. *Phys. Rev. Lett.* **105**, 136805 (2010).
- Splendiani, A. *et al.* Emerging photoluminescence in monolayer  $\text{MoS}_2$ . *Nano Lett.* **10**, 1271–1275 (2010).
- Wilson, J. A. & Yoffe, A. D. The transition metal dichalcogenides discussion and interpretation of the observed optical, electrical and structural properties. *Adv. Phys.* **18**, 193–335 (1969).
- Gutiérrez, H. R. *et al.* Extraordinary room-temperature photoluminescence in triangular  $\text{WS}_2$  monolayers. *Nano Lett.* **13**, 3447–3454 (2013).
- Bernardi, M., Palumbo, M. & Grossman, J. C. Extraordinary sunlight absorption and one nanometer thick photovoltaics using two-dimensional monolayer materials. *Nano Lett.* **13**, 3664–3670 (2013).
- Zhao, W. *et al.* Evolution of electronic structure in atomically thin sheets of  $\text{WS}_2$  and  $\text{WSe}_2$ . *ACS Nano* **7**, 791–797 (2013).
- Mak, K. F., He, K., Shan, J. & Heinz, T. F. Control of valley polarization in monolayer  $\text{MoS}_2$  by optical helicity. *Nat. Nanotechnol.* **7**, 494–498 (2012).
- Zeng, H., Dai, J., Yao, W., Xiao, D. & Cui, X. Valley polarization in  $\text{MoS}_2$  monolayers by optical pumping. *Nat. Nanotechnol.* **7**, 490–493 (2012).
- Li, Y. *et al.* Probing symmetry properties of few-layer  $\text{MoS}_2$  and h-BN by optical second-harmonic generation. *Nano Lett.* **13**, 3329–3333 (2013).
- Mak, K. F. *et al.* Tightly bound trions in monolayer  $\text{MoS}_2$ . *Nat. Mater.* **12**, 207–211 (2013).
- Xiao, D., Liu, G.-B., Feng, W., Xu, X. & Yao, W. Coupled spin and valley physics in monolayers of  $\text{MoS}_2$  and other group-VI dichalcogenides. *Phys. Rev. Lett.* **108**, 196802 (2012).
- Zhu, Z. Y., Cheng, Y. C. & Schwingschlögl, U. Giant spin-orbit-induced spin splitting in two-dimensional transition-metal dichalcogenide semiconductors. *Phys. Rev. B* **84**, 153402 (2011).
- Li, T. & Galli, G. Electronic Properties of  $\text{MoS}_2$  Nanoparticles. *J. Phys. Chem. C* **111**, 16192–16196 (2007).
- Duerloo, K.-A. N., Li, Y. & Reed, E. J. Structural phase transitions in two-dimensional Mo- and W-dichalcogenide monolayers. *Nat. Commun.* **5**, 4214 (2014).
- Ghorbani-Asl, M. *et al.* Electromechanics in  $\text{MoS}_2$  and  $\text{WS}_2$ ; nanotubes vs. monolayers. *Sci. Rep.* **3**, 2961 (2013).
- Hofmann, W. K. Thin films of molybdenum and tungsten disulphides by metal organic chemical vapour deposition. *J. Mater. Sci.* **23**, 3981–3986 (1988).
- Reale, F., Sharda, K. & Mattevi, C. From bulk crystals to atomically thin layers of group VI-transition metal dichalcogenides vapour phase synthesis. *Applied Materials Today* **3**, 11–22 (2016).
- Rong, Y. *et al.* Controlling sulphur precursor addition for large single crystal domains of  $\text{WS}_2$ . *Nanoscale* **6**, 12096–12103 (2014).
- Zhang, Y. *et al.* Controlled growth of high-quality monolayer  $\text{WS}_2$  layers on sapphire and imaging its grain boundary. *ACS Nano* **7**, 8963–8971 (2013).
- Eliás, A. L. *et al.* Controlled synthesis and transfer of large-area  $\text{WS}_2$  sheets: from single layer to few layers. *ACS Nano* **7**, 5235–5242 (2013).
- Xu, Z. Q. *et al.* Synthesis and transfer of large-area monolayer  $\text{WS}_2$  crystals: moving toward the recyclable use of sapphire substrates. *ACS Nano* **9**, 6178–6187 (2015).
- Fu, Q. *et al.* Controllable synthesis of high quality monolayer  $\text{WS}_2$  on a  $\text{SiO}_2/\text{Si}$  substrate by chemical vapor deposition. *RSC Adv.* **5**, 15795–15799 (2015).
- Lee, Y. H. *et al.* Synthesis and transfer of single-layer transition metal disulfides on diverse surfaces. *Nano Lett.* **13**, 1852–1857 (2013).
- Kang, K. *et al.* High-mobility three-atom-thick semiconducting films with wafer-scale homogeneity. *Nature* **520**, 656–660 (2015).
- Gao, Y. *et al.* Large-area synthesis of high-quality and uniform monolayer  $\text{WS}_2$  on reusable Au foils. *Nat. Commun.* **6**, 8569 (2015).
- Cudennec, Y. & Lecerf, A. Topotactic transformations of goethite and lepidocrocite into hematite and maghemite. *Solid State Sci.* **7**, 520–529 (2005).
- Okada, M. *et al.* Direct chemical vapor deposition growth of  $\text{WS}_2$  atomic layers on hexagonal boron nitride. *ACS Nano* **8**, 8273–8277 (2014).
- Bosi, M. Growth and synthesis of mono and few-layers transition metal dichalcogenides by vapour techniques: a review. *RSC Adv.* **15**, 75500–75518 (2015).
- Shi, Y., Lib, H. & Li, L.-J. Recent advances in controlled synthesis of two-dimensional transition metal dichalcogenides via vapour deposition techniques. *Chem. Soc. Rev.* **44**, 2744–2756 (2015).
- Li, S. *et al.* Halide-assisted atmospheric pressure growth of large  $\text{WSe}_2$  and  $\text{WS}_2$  monolayer crystals. *Applied Materials Today* **1**, 60–66 (2015).
- Kim, H. *et al.* Activation energy paths for graphene nucleation and growth on Cu. *ACS Nano* **6**, 3614–3623 (2012).
- McKone, J. R., Pieterick, A. P., Gray, H. B. & Lewis, N. S. Hydrogen evolution from Pt/Ru-coated p-type  $\text{WSe}_2$  photocathodes. *JACS* **135**, 223–231 (2013).
- Baglio, J., Kamiñiecki, E., DeCola, N. & Struck, C. Growth and characterization of n- $\text{WS}_2$  and niobium-doped p- $\text{WS}_2$  single crystals. *J. Solid State Chem.* **49**, 166–179 (1983).
- Gäggeler, H. W. & Türler, A., *Gas-Phase Chemistry of Superheavy Elements. The Chemistry of Superheavy Elements* (2th ed.) (2013).
- Kim, H., Saiz, E., Chhowalla, M. & Mattevi, C. Modeling of the self-limited growth in catalytic chemical vapor deposition of graphene. *New J. Phys.* **15**, 053012 (2013).
- Carmalt, C. J., Parkin, I. P. & Peters, E. S. Atmospheric pressure chemical vapour deposition of  $\text{WS}_2$  thin films on glass. *Polyhedron* **22**, 1499–1505 (2003).
- Withers, F., Bointon, T. H., Hudson, D. C., Craciun, M. F. & Russo, S. Electron transport of  $\text{WS}_2$  transistors in a hexagonal boron nitride dielectric environment. *Sci. Rep.* **4**, 4967 (2014).
- Berkdemir, A. *et al.* Identification of individual and few layers of  $\text{WS}_2$  using Raman Spectroscopy. *Sci. Rep.* **3**, 1775 (2013).

39. Wu, R. J., Wu, R. J., Odlyzko, M. L. & Mkhoyan, K. A. Determining the thickness of atomically thin MoS<sub>2</sub> and WS<sub>2</sub> in the TEM. *Ultramicroscopy* **147**, 8–20 (2014).
40. Rasmussen, F. A. & Thygesen, K. S. Computational 2D materials database: electronic structure of transition-metal dichalcogenides and oxides. *J. Phys. Chem. C* **119**, 13169–13183 (2015).
41. Liu, H. *et al.* Fluorescence concentric triangles: a case of chemical heterogeneity in WS<sub>2</sub> atomic monolayer. *Nano Lett.* **16**, 5559–5567 (2016).
42. Tongay, S. *et al.* Defects activated photoluminescence in two-dimensional semiconductors: interplay between bound, charged, and free excitons. *Sci. Rep.* **3**, 2657 (2013).
43. Cattelan, M. *et al.* New strategy for the growth of complex heterostructures based on different 2D materials. *Chem. Mater.* **27**, 4105–4113 (2015).
44. Martinez, H. *et al.* Influence of the cation nature of high sulfur content oxysulfide thin films MOySz (M = W, Ti) studied by XPS. *Appl. Surf. Sci.* **236**, 377–386 (2004).
45. Yun, S. J. *et al.* Synthesis of centimeter-scale monolayer tungsten disulfide film on gold foils. *ACS Nano* **9**, 5510–5519 (2015).
46. Alharbi, A. & Shahrjerdi, D. Electronic properties of monolayer tungsten disulfide grown by chemical vapor deposition. *Appl. Phys. Lett.* **109**, 193502 (2016).
47. Lan, C., Li, C., Yina, Y. & Liu, Y. Large-area synthesis of monolayer WS<sub>2</sub> and its ambient sensitive photo-detecting performance. *Nanoscale* **7**, 5974–5980 (2015).
48. Hussain, A. M., Torres Sevilla, G. A., Rader, K. R. & Hussain, M. M. Chemical vapor deposition based tungsten disulfide (WS<sub>2</sub>) thin film transistor. *SIECP*. <https://doi.org/10.1109/SIECP.2013.6550981> (2013).
49. Cui, Y. *et al.* High-performance monolayer WS<sub>2</sub> field-effect transistors on high-κ dielectrics. *Adv. Mater.* **27**, 5230–5234 (2015).
50. Iqbal, M. W. *et al.* Tailoring the electrical and photo-electrical properties of a WS<sub>2</sub> field effect transistor by selective n-type chemical doping. *RSC Adv.* **6**, 24675–24682 (2016).
51. Georgiou, T. *et al.* Electrical and optical characterization of atomically thin WS<sub>2</sub>. *Dalton Trans.* **43**, 10388–10391 (2014).
52. Iqbal, M. W. *et al.* Deep-ultraviolet-light-driven reversible doping of WS<sub>2</sub> field-effect transistors. *Nanoscale* **7**, 747–757 (2015).
53. Ovchinnikov, D., Allain, A., Huang, Y.-S., Dumcenco, D. & Kis, A. Electrical transport properties of single-layer WS<sub>2</sub>. *ACS Nano* **8**, 8174–8181 (2014).
54. Jo, S., Ubrig, N., Berger, H., Kuzmenko, A. B. & Morpurgo, A. F. Mono- and bilayer WS<sub>2</sub> light-emitting transistors. *Nano Lett.* **14**, 2019–2025 (2014).

## Acknowledgements

C.M. would like to acknowledge the EPSRC awards EP/K033840/1, EP/K01658X/1, EP/K016792/1, EP/M022250/1, the EPSRC-Royal Society Fellowship Engagement Grant EP/L003481/1 and the award of a Royal Society University Research Fellowship by the UK Royal Society. N.N. acknowledge the Imperial College Junior Research Fellowship and P.C.S. would like to acknowledge the funding and support from the European Commission (H2020 – Marie Skłodowska Curie European Fellowship–660721). I.A. acknowledges financial support from The European Commission Marie Curie Individual Fellowships (Grant number 701704). J.D.M. acknowledges the financial support from the Engineering and Physical Sciences Research Council (EPSRC) of the United Kingdom, via the EPSRC Centre for Doctoral Training in Metamaterials (Grant No. EP/L015331/1). S.R. and M.F.C. acknowledge financial support from EPSRC (Grant no. EP/J000396/1, EP/K017160/1, P/K010050/1, EP/G036101/1, EP/M001024/1, EP/M002438/1), from Royal Society international Exchanges scheme 2016/R1 and from The Leverhulme trust (grant title “Quantum Drums” and “Room temperature quantum electronics”).

## Author Contributions

C.M. conceived the idea, C.M. and F.R. designed the experiments. F.R. performed the syntheses of WS<sub>2</sub> and analysed the data. P.P. performed Raman and photoluminescence characterization and data analysis. I.A., G.F.J., J.D.M. and A.B. fabricated the FETs and performed electrical characterization and data analysis under the supervision of S.R. and M.C. N.N. performed TEM characterization. P.C.S. performed XRD characterization. S.A. performed XPS characterization. F.R. and C.M. prepared the manuscript and all authors reviewed the manuscript. All the authors have read the manuscript and agree with its content.

## Additional Information

**Supplementary information** accompanies this paper at <https://doi.org/10.1038/s41598-017-14928-2>.

**Competing Interests:** The authors declare that they have no competing interests.

**Publisher's note:** Springer Nature remains neutral with regard to jurisdictional claims in published maps and institutional affiliations.



**Open Access** This article is licensed under a Creative Commons Attribution 4.0 International License, which permits use, sharing, adaptation, distribution and reproduction in any medium or format, as long as you give appropriate credit to the original author(s) and the source, provide a link to the Creative Commons license, and indicate if changes were made. The images or other third party material in this article are included in the article's Creative Commons license, unless indicated otherwise in a credit line to the material. If material is not included in the article's Creative Commons license and your intended use is not permitted by statutory regulation or exceeds the permitted use, you will need to obtain permission directly from the copyright holder. To view a copy of this license, visit <http://creativecommons.org/licenses/by/4.0/>.

© The Author(s) 2017